JOURNAL OF MATERIALS SCIENCE **39** (2004) 4809–4819

Mechanical and thermal properties of physical vapour deposited alumina films

Part II *Elastic, plastic, fracture, and adhesive behaviour*

J. THURN[†], R. F. COOK[*]
Department of Chemical Engineering and Materials Science, University of Minnesota,
Minneapolis, MN 55455, USA
E-mail: rfc@cems.umn.edu

Two mechanical characterization techniques were used to deduce the elastic, plastic, fracture, and adhesive properties of non-reactive physical vapour deposited alumina films of varying thickness on Al_2O_3-TiC substrates deposited at two different substrate biases. Depth-sensing indentation at both nano- and macroscopic load scales was used to determine the elastic and plastic properties of the films. Gravity-loaded Vickers indentation was performed to examine the fracture properties of the film and of the interface. Novel fracture mechanics models were developed to describe indentation-induced film fracture by channel cracks and indentation-induced interface delamination. The former model was used to determine the film toughness and the latter model was used to deduce the interfacial fracture resistance of the films and correctly predicted the effect of changing film thickness. Both models described the measured crack lengths with indentation load well and were used to identify the transition from radial and lateral cracking to channel and interfacial cracking.

1. Introduction

The thermal stability of physical vapour deposited (PVD) alumina (AlO_x) films was examined in the preceding paper (hereafter referred to as Part I) [1]. Nonlinear hysteretic compressive stress development during thermal cycling and annealing was found to induce film delamination, through-film cracking, and chipping. This paper continues the examination of thermally-induced AlO_x film failure by investigating the film contact response. Vickers indentation was used to characterize the elasto-plastic, adhesion, and fracture properties of sputtered alumina films on Al_2O_3-TiC substrates. A single indentation event caused permanent plastic deformation (the residual impression), film cracking (above a threshold load), and delamination from the Al_2O_3-TiC substrate (above another threshold load), as shown in the indentation sequence of Fig. 1. The indentation loads of Fig. 1a–e are 4, 5, 8, 18 and 33 N, respectively, and show a residual impression, radial and lateral cracks at the smaller threshold load, delamination at the larger threshold load, the onset of asymmetrical (and possibly unstable) delamination, and chipping, respectively, on a 16 μm film deposited at -130 V. Because so many phenomena occurred in the films on indentation, it was the primary characterization technique used in this study. Film stress results (deposition and thermal) from Part I were obtained using a substrate curvature measurement technique and depth-sensing indentation (DSI) was performed to measure film modulus.

2. Analysis

2.1. Depth-sensing indentation

Load-displacement (P-h) traces were obtained from DSI experiments, in which the load P and displacement h are measured continuously throughout an indentation event. A schematic diagram of the indentation process is shown in Fig. 2. The indenter, of included angle 2α, is in contact with the material to a displacement $h_c (< h$ for brittle materials) with a contact diagonal of $2a$ (Fig. 2a). A typical P-h trace is shown in Fig. 3. On loading the material deforms both elastically and plastically. At peak load, P_{max}, the indenter displacement is h_{max}. On unloading, the material deforms only elastically and some of the depth h_{max} is recovered. On complete unload the material has been permanently deformed and is left with a residual indentation impression of depth h_f (Fig. 2b). It has been observed experimentally (on transparent ceramics) that the impression diagonals do not recover on unloading and only the depth of the impression recovers [2]. Cracks are initiated at

---

[*] Author to whom all correspondence should be addressed.

[†] *Present address:* Advanced Mechanical Technology, Mechanical Research and Development, Seagate Technology, Bloomington, MN 55435, USA.

0022–2461 © *2004 Kluwer Academic Publishers*

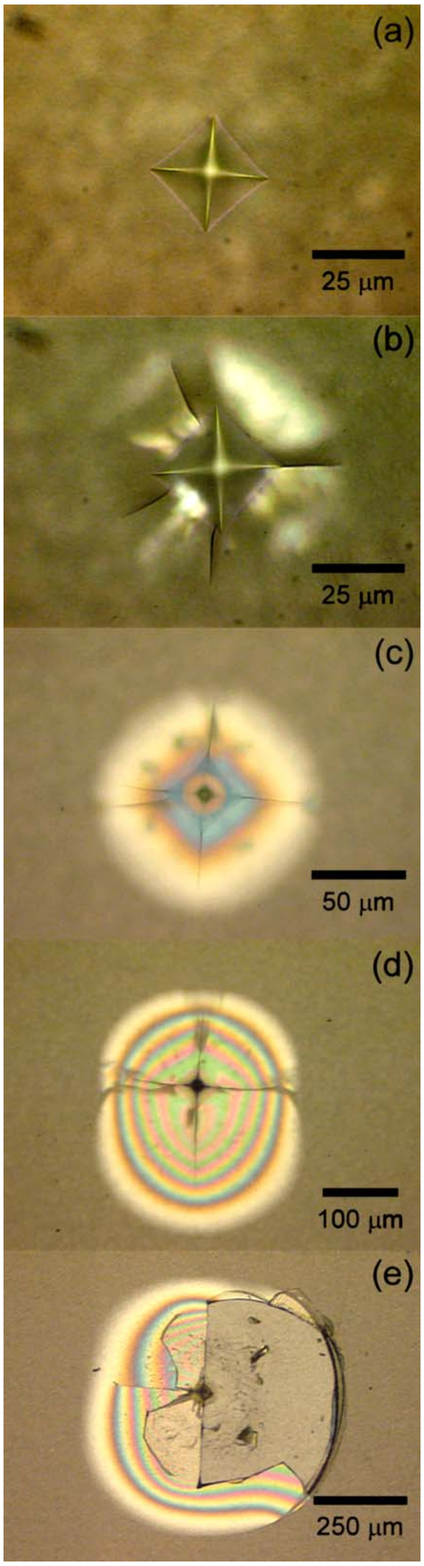

Figure 1 Vickers indentations on AH3, a 16 μm AlO_x film deposited at a substrate bias of -130 V on Al_2O_3-TiC. The indentation loads of (a)–(e) are 4, 5, 8, 18 and 33 N, respectively. Features of interest are: (a) residual impression, (b) radial and lateral cracking, (c) delamination and channel cracking, (d) asymmetrical delamination with channel cracking, and (e) chipping. Note the Al_2O_3-TiC surface in (e) is crack-free, indicating that the channel cracks were confined to the film.

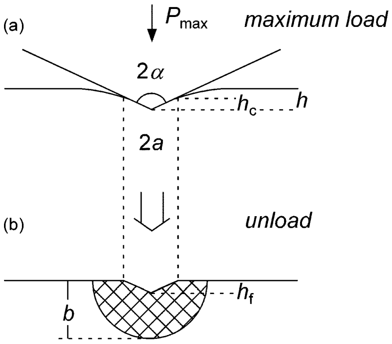

Figure 2 Schematic cross-section of the indentation event: (a) during loading and (b) following complete unload.

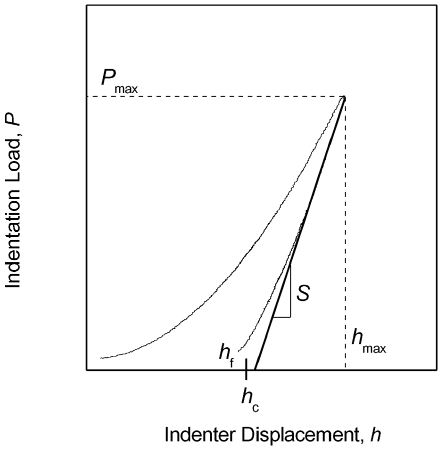

Figure 3 Representative load-displacement (P-h) trace. Parameters used in deconvoluting P-h traces to obtain material properties are indicated.

the corners of the contact during unloading, driven by the residual field associated with the localized "plastic zone" beneath the impression. Typically, half-penny or radial cracks that intersect the surface of the material are generated during loading or the early stages of unloading while lateral cracks (located under the plastic zone parallel to the surface) initiate at almost complete unload [3].

The P-h traces can be used to determine the indentation hardness H and plane-strain modulus $E^* = E/(1-\nu^2)$ of the film. By definition indentation hardness is

$$H = \frac{P_{\max}}{A_p}, \tag{1}$$

where A_p is the projected contact area at peak load. As mentioned above for brittle materials, the diagonals of the residual impression do not recover on unloading, so post-indentation measurement of the corner-to-corner distance $2a$ provides an estimate of $A_p = 2a^2$ for Vickers indentations. The projected contact area can also be estimated from the contact depth h_c using the procedure outlined in Oliver and Pharr [4]. The modulus is related to the unloading stiffness S (Fig. 3) and A_p by:

$$E_r = \frac{\pi^{1/2}}{2}\frac{S}{A_p^{1/2}}, \tag{2}$$

where E_r is the reduced modulus

$$E_r = \left(\frac{(1-\nu^2)}{E} + \frac{(1-\nu_i^2)}{E_i}\right)^{-1}. \tag{3}$$

E_i and ν_i are the modulus and Poisson's ratio of the diamond indenter tip, taken here to be 1141 GPa and 0.07, respectively.

The modulus and hardness of a film-substrate system vary with indentation load. Here they will be reported as functions of the relative contact depth, h_c/t_f, where t_f is the film thickness. Typically the calculated modulus is representative of the film and free of any effects of the substrate if $h_c/t_f < 0.2$ [5, 6] and the calculated hardness if $h_c/t_f < 0.7$ [6]. Finite element simulations of the indentation event on brittle materials imply that cracking during loading or unloading should not be expected to influence the measured modulus or hardness [7].

2.2. Vickers indentation

2.2.1. Indentation-induced film cracking

Vickers indentation has long been used to estimate the toughness of brittle materials using models developed for either half-penny [8] or radial cracks [9]. Fig. 4 shows a schematic plan-view of a Vickers indentation event. The residual impression diagonal is $2a$ and the surface traces of cracks emanating from the corners of the impression are of length c_0 (at equilibrium). A cross-sectional view of the residual impression of Fig. 4 is shown in Fig. 5a, where the surface traces are assumed to be due to radial cracking. Radial cracks initiate at the corners of the indentation impression and are semi-elliptical in shape. They are driven by the hydrostatic pressure of the plastic zone, shown as a hemi-sphere of radius b under the residual impression. Radial cracks rarely extend in depth beneath the plastic zone [3]. For cracks of this type (or half-penny cracks) the stress-intensity factor K is [8]:

$$K = 2\xi (EH)^{1/2} \frac{a^2}{c^{3/2}}, \tag{4}$$

where ξ is a constant of magnitude 0.022 [10]. Typically films are deposited in a state of stress (tensile or compressive) and this serves as an additional driving force for film fracture. This can be accounted for by using [11]:

$$K = \psi \sigma_f c^{1/2}, \tag{5}$$

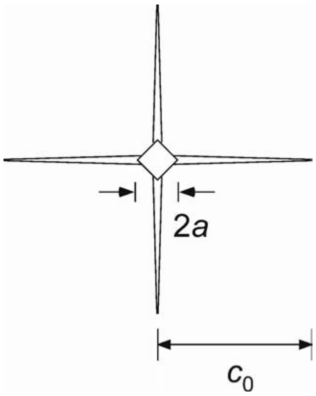

Figure 4 Schematic plan-view of a Vickers indentation event.

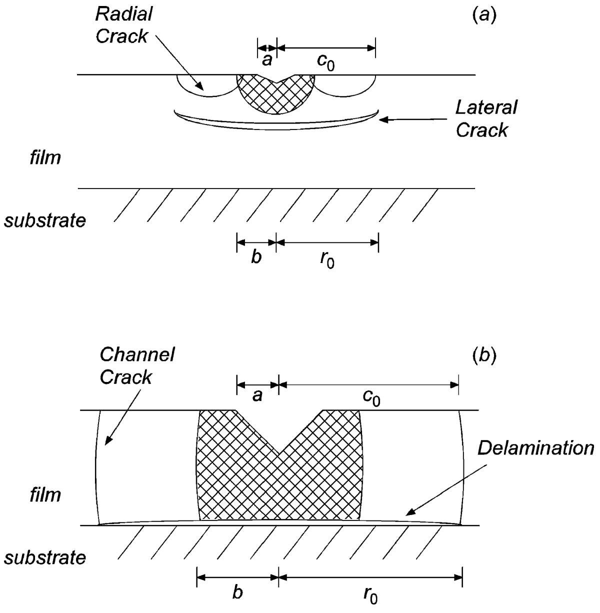

Figure 5 Schematic cross-section of a Vickers indentation event in a film. (a) The contact-induced deformation and fracture is unaffected by the substrate. The plastic zone is spherical in shape, the surface traces result from radial cracks, and lateral cracking occurs beneath the plastic zone. (b) The contact-induced deformation and fracture is constrained by the harder, tougher substrate. The plastic zone is cylindrical in shape, the surface traces result from channel cracks, and delamination occurs at the interface.

where $\psi = 1.21$ for a radial crack. At equilibrium, Equations 4 and 5 can be combined to estimate the film toughness, T (at equilibrium $K = T$), from a single measurement of the equilibrium crack length c_0 and a:

$$T = 2\xi (EH)^{1/2} \frac{a^2}{c_0^{3/2}} + \psi \sigma_f c_0^{1/2}. \tag{6}$$

Similarly the toughness may be used to predict crack lengths by re-arranging Equation 6 to get:

$$T c_0^{3/2} - \psi \sigma_f c_0^2 = 2\xi (EH)^{1/2} a^2. \tag{7}$$

Note that if there is no film stress, Equation 7 predicts $c_0 \sim a^{4/3}$ and a logarithmic plot of c_0 against a should be a straight line of slope 4/3. This model works well for homogeneous ceramics and in this study will be applied to small-load indentations on thick films.

For large-load indentations on thick films or indentations on thin films, the plastic zone and radial cracks begin to interact with the substrate. If the substrate is harder and tougher than the film, then the plastic zone and film cracks will develop into the geometries shown in Fig. 5b. This is expected to be the case in this study, as the reported hardness and toughness of the Al_2O_3-TiC substrates are: $H = 23$ GPa [12] and $T = 6.6$ MPa m$^{1/2}$ [13]. When confronted with the interface, the plastic zone can no longer retain its hemi-spherical shape as it cannot extend into the hard substrate and so develops a cylindrical or barrel-like shape of radius b. The radial cracks also cannot extend into the tougher substrate but continue to grow away from the plastic zone, developing into channel cracks of length c_0. A model describing channel cracks driven by the plastic field is developed here in a manner consistent with Lawn *et al.* [8] and a previous analysis of roller indentation-induced median cracks [14].

The hydrostatic pressure P^{I} in the cylindrical plastic zone can be estimated from the volume displaced by the residual contact impression ΔV:

$$\Delta V = \frac{A_{\mathrm{p}} h_{\mathrm{f}}}{3}. \tag{8}$$

If we define $\varepsilon = h_{\mathrm{f}}/h_{\max}$ (see Fig. 3) then Equation 8 can be written as

$$\Delta V = \frac{A_{\mathrm{p}} h_{\max}\varepsilon}{3} = \frac{2\varepsilon a^3}{3\tan\alpha}, \tag{9}$$

using $A_{\mathrm{p}} = 2a^2$ for a Vickers indenter and $\tan\alpha = a/h_{\max}$ for a conical indenter ($\alpha = 74^\circ$ for an ideal Vickers indenter). The hydrostatic pressure is:

$$P^{\mathrm{I}} = d_1 \kappa \frac{\Delta V}{V_{\mathrm{p}}}, \tag{10}$$

where $V_{\mathrm{p}} = \pi t_{\mathrm{f}} b^2$ is the volume of the cylindrical plastic zone, κ is the bulk modulus of the film, and d_1 is a constant (of order one or less). This pressure acts as an opening line force on the channel crack. The stress-intensity factor for a one-dimensional linear crack under line loading is [15]:

$$K = \frac{P_{\mathrm{L}}}{(\pi c)^{1/2}}, \tag{11}$$

where P_{L} is the line force per unit thickness of the crack. The line force is related to the hydrostatic pressure by $P_{\mathrm{L}} = d_2 b P^{\mathrm{I}}$, where d_2 is a constant. Finally, from Hill's analysis of expanding cylindrical cavities [16]:

$$\frac{b}{a} = d_3 \left(\frac{E_{\mathrm{f}}}{H_{\mathrm{f}}}\right)^{2/3} \cot^{1/2}\alpha, \tag{12}$$

where d_3 is a constant that includes the magnitude of hardness and stiffness mis-match between the film and substrate. Combining Equations 9 through 12 results in the following expression for the stress-intensity factor:

$$K = \left[\frac{2 d_1 d_2 \varepsilon}{9\pi^{3/2}(1-2\nu) d_3 \tan^{1/2}\alpha}\right] \frac{\left(E_{\mathrm{f}} H_{\mathrm{f}}^2\right)^{1/3}}{t_{\mathrm{f}}} \frac{a^2}{c^{1/2}}, \tag{13}$$

and the constant term in brackets will be labelled λ. As before, film stress provides an additional driving force for film fracture. In the case of channel cracks, the stress-intensity factor is [17]:

$$K = \psi \sigma_{\mathrm{f}} t_{\mathrm{f}}^{1/2}, \tag{14}$$

where ψ depends on the stiffness mis-match of the film and substrate [18]. At equilibrium, Equations 13 and 14 can be combined to estimate the film toughness:

$$T = \lambda \frac{\left(E_{\mathrm{f}} H_{\mathrm{f}}^2\right)^{1/3}}{t_{\mathrm{f}}} \frac{a^2}{c_0^{1/2}} + \psi \sigma_{\mathrm{f}} t_{\mathrm{f}}^{1/2}. \tag{15}$$

Equation 15 can be re-arranged to give the variation of equilibrium channel crack length with indentation impression dimension:

$$c_0 = \left[\frac{\lambda \left(E_{\mathrm{f}} H_{\mathrm{f}}^2\right)^{1/3}}{t_{\mathrm{f}}\left(T - \psi \sigma_{\mathrm{f}} t_{\mathrm{f}}^{1/2}\right)}\right]^2 a^4, \tag{16}$$

suggesting that a logarithmic plot of c_0 against a should be a straight line of slope four. If the threshold for radial cracking is small enough, it will be possible to use both models (Equations 6 and 15) to determine the toughness of a film as the crack evolves from a fully developed radial crack at small loads (Fig. 5a) to a fully developed channel crack at large loads (Fig. 5b). The transition should occur as the substrate begins to interfere with the plastic zone development. This should be identifiable by the so-called substrate effect on indentation hardness, at which H begins to increase from the film value at $h_{\mathrm{c}}/t_{\mathrm{f}} \approx 0.7$ [6]. Fig. 6a shows the expected transition from radial to channel cracking (assuming $\sigma_{\mathrm{f}} = 0$) as the contact dimension (and relative contact depth) increases.

2.2.2. Indentation-induced interfacial fracture

Fracture beneath the plastic zone parallel to the free surface (lateral cracking) is evident in Fig. 1b and shown

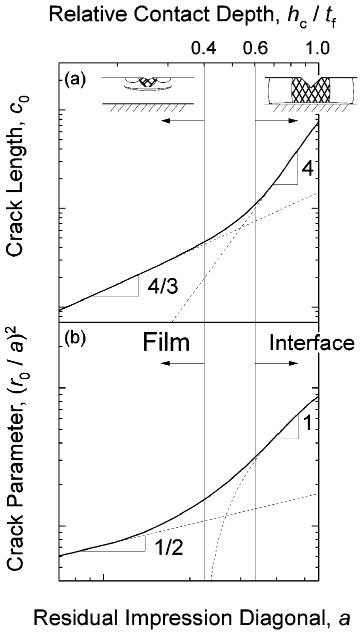

Figure 6 The constraining effect of a hard, stiff substrate on indentation-induced cracking assuming $\sigma_{\mathrm{f}} = 0$. (a) Transition from radial ($c_0 \sim a^{4/3}$) to channel ($c_0 \sim a^4$) cracking. (b) Transition from lateral [$(r_0/a)^2 \sim a^{1/2}$] to interfacial cracking. Asymptotes are shown as dashed lines. For interfacial cracking, the crack parameter $(r_0/a)^2$ is linear in a but does not pass through the origin, so this asymptote appears nonlinear plotted on logarithmic scales.

schematically in Fig. 5a. Although the radius of lateral cracks, r_0, can be difficult to measure, a relationship between r_0 and a has been identified [19] and can be written as (using $H = P/2a^2$):

$$r_0 = \left[\frac{32^{1/4}\zeta_L}{(\tan\alpha)^{5/6}}\frac{(E^3H)^{1/4}}{T}\right]^{1/2} a^{5/4}, \tag{17}$$

where ζ_L is a constant. This relationship can be written in terms of $(r_0/a)^2$, termed the "interfacial crack parameter," which will be important later:

$$\left(\frac{r_0}{a}\right)^2 = \left[\frac{32^{1/4}\zeta_L}{(\tan\alpha)^{5/6}}\frac{(E^3H)^{1/4}}{T}\right] a^{1/2}. \tag{18}$$

As a increases and the lateral cracks approach the substrate, they are confined to the weak interface (Fig. 5b) and the scaling of Equation 18 no longer applies.

Fracture at the film-substrate interface can be identified in Fig. 1 by the appearance of circular interference fringes above a threshold indentation load. This axisymmetric interface crack is, like the radial and channel cracks, driven by the hydrostatic pressure of the plastic zone. The mechanical energy release rate G derived by Thouless [20] for an edge-loaded axisymmetric interface crack applies to the geometry depicted in Fig. 7:

$$G = \frac{2\left(1-\nu_f^2\right)(P^I)^2 t_f}{E_f\left[(1+\nu_f) + \left(\frac{r}{b}\right)^2(1-\nu_f)\right]^2}, \tag{19}$$

where r is the radius of the interfacial crack. Equations 9, 10 and 12 can be combined with Equation 19 to get (at equilibrium, $G = R$ [21]):

$$\left(\frac{r_0}{a}\right)^2 = \Lambda\left(\frac{E_f}{Rt_f}\right)^{1/2} a - \frac{1+\nu_f}{1-\nu_f}\left(\frac{E_f}{H_f}\right)^{4/3}\frac{d_3^2}{\tan\alpha}, \tag{20}$$

where

$$\Lambda = \left(\frac{8(1+\nu_f)d_1^2\varepsilon^2}{81\pi^2(1-2\nu_f)^2(1-\nu_f)\tan^2\alpha}\right)^{1/2} \tag{21}$$

is another geometrical constant and R is the fracture resistance of the interface. By comparison with Equation 18, interfacial cracks have a stronger dependence on the contact dimension than do lateral cracks. Fig. 6b shows the expected transition of the interfacial crack parameter as fully-developed lateral cracks transform to fully-developed interfacial cracks.

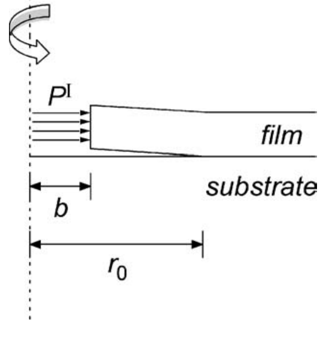

Figure 7 Schematic cross-section of edge-stress driven axisymmetric interfacial cracking.

The model above can be compared with a similar scaling predicted by Marshall and Evans for indentation-induced interfacial fracture [22]:

$$\left(\frac{r_0}{a}\right)^2 = \Lambda^*\left(\frac{E_f}{Rt_f}\right)^{1/2} a, \tag{22}$$

where

$$\Lambda^* = \left(\frac{(1+\nu_f)\varepsilon^2}{18\pi^2(1-\nu_f)\tan^2\alpha}\right)^{1/2}. \tag{23}$$

The similarity between the two models is striking: the only difference between them is Equation 20 is offset from the origin by a constant and Equation 22 passes through the origin (also the values of Λ and Λ^* are slightly different). The differences arise from the choice of boundary conditions; Equation 20 constrains the displacement at the edge of the delamination r_0 while Equation 22 enforces a condition of zero stress at r_0 [20, 22].

Note that the film stress does not enter either Equation 20 or Equation 22 because the films are assumed to be delaminated but not buckled. Buckling typically requires compressive film stresses on the order of hundreds of MPa or greater, a circumstance not expected here [1]. A quantitative condition for buckling was provided in Marshall and Evans based on the equivalent edge stress acting along the circumference of the delaminated region [22],

$$\sigma_0 = \frac{E_f\varepsilon}{3\pi(1-\nu_f)\tan\alpha t_f}\frac{a^3}{r^2}. \tag{24}$$

Buckling occurs then if $\sigma_0 + \sigma_f < \sigma_c$ (compressive stresses are negative), where

$$\sigma_c = \frac{kE_f t_f^2}{12\left(1-\nu_f^2\right)}\frac{1}{r^2} \tag{25}$$

is the critical buckling stress. k is a buckling parameter and equal to 14.68 for a clamped plate with the maximum deflection at the centre of the plate and 42.67 for a clamped plate constrained to have zero deflection at the centre of the plate [23]. Rossington *et al.* [24] successfully used the relative unbuckled and buckled delamination of sputtered ZnO films on Si to measure the interfacial crack resistance, and Kriese *et al.* [25] used the buckled response directly (measuring ε by DSI) to determine the interfacial crack resistance of sputtered Cu films on thermal SiO_2.

3. Experimental procedure

Deposition conditions and the specimen naming scheme are provided in Part I. DSI at ultra-microscopic scales (“nanoindentation”) was performed with a commercial load-controlled instrument (Nanoindenter XP, MTS Systems Corp.) with a Berkovich tip and macroscopic scale DSI with a custom-built apparatus with a Vickers tip, described in Ref. [2]. Both machines were calibrated on standard ceramic materials using a two-parameter area function relating A_p to h_c [26].

Vickers indentation was performed using commercial gravity-loaded machines (Beuhler and Zwick) at peak loads ranging from 0.1 to 33 N. At least ten indentations were made at each peak load on each specimen.

4. Results and discussion

4.1. Depth-sensing indentation

DSI was used to estimate the film plane-strain modulus and hardness by deconvolution of the *P-h* trace as described in Oliver and Pharr [4] using both nano- and macroindentation. Fig. 8a shows macroindentation *P-h* traces on specimen AH3. The unloading stiffness increases with increasing contact depth as a result of (i) increasing contact area and (ii) the increasing effect of the stiff substrate. Included in Fig. 8a is a *P-h* trace from indentation of (0001) sapphire. Clearly, the AlO_x film is less stiff than bulk crystalline Al_2O_3. (The contact responses of polycrystalline Al_2O_3 and Al_2O_3-TiC are similar to the *P-h* trace shown for sapphire.) Fig. 8b shows the modulus (left ordinate, circles) and hardness (right ordinate, diamonds) of AH3 with relative contact depth. The uncertainty bars on the nanoindentation measurements (open symbols) represent the standard deviation of at least five indentations while only a single macroindentation measurement (solid symbol) was performed at each depth. The plane-strain modulus is approximately constant for $h_c/t_f < 0.2$ at $E_f^* = 165 \pm 10$ GPa (or $E_f = 158$ GPa if $\nu_f = 0.2$) but then increased, as previously observed for relatively compliant films on stiff substrates [27–31]. The hardness value differs when measured by nanoindentation and macroindentation. The nanoindentation hardness is 9.1 ± 0.4 GPa and the conventional hardness is 7.5 ± 0.5 GPa from macroindentations taken from data for $h_c/t_f < 0.4$. This phenomenon, in which the nanoindentation hardness differs from the conventional, or macroscopically measured hardness, has been observed before on select materials (most notably fused silica) [4, 32, 33] but this does not prohibit the hardness from being used as a comparison between the films deposited at different substrate biases. Above a relative contact depth of 0.4, the hardness begins to slowly increase towards that of the substrate ($H = 23$ GPa).

Fig. 9a shows the macroindentation *P-h* traces for AL1. Similar to AH3, AL1 was less stiff than its bulk counterpart, Al_2O_3, and exhibited an increased stiffness with increasing contact depth. Fig. 9b shows the modulus and hardness of AL1 with trends similar to that observed in Fig. 8b. From indentations for $h_c/t_f < 0.2$, $E_f^* = 181 \pm 10$ GPa (or $E_f = 174$ GPa if $\nu_f = 0.2$). The nanoindentation hardness is 9.7 ± 0.8 GPa and conventional hardness 8.1 ± 0.2 GPa from indentations at relative contact depths less than 0.4, although the increase with increasing contact depth is negligible. The moduli and nanoindentation hardness obtained for both films are similar to other nanoindentation studies on sputtered amorphous AlO_x films [34]. Both the hardness and plane-strain modulus (Table I) obtained by DSI are greater for the films deposited at a substrate bias −50 V than for the films deposited at a substrate bias of −130 V.

The elastic moduli determined by DSI were used in conjunction with the thermal stress data to estimate the film CTE using Equation 3 of Part I. The CTE can be obtained from the linear stress-temperature response obtained after the first cycle to a peak temperature (Table I of Part I). The calculated CTE are listed in Table I for all thermally cycled films for the cycles to 300°C following the anneal and from the cycles to peak temperatures of 100, 200, 300, 400 and 500°C for AH1. In all cases, as expected from the thermal stability plots of Part I, the CTE is nearly matched to or slightly less than that of the Al_2O_3-TiC substrate. For AH1 it decreases during the heat treatment, as suggested by the change in the slope of the thermal stress response with increasing peak temperature (Part I). The CTE of the films deposited at a substrate bias of −50 V are

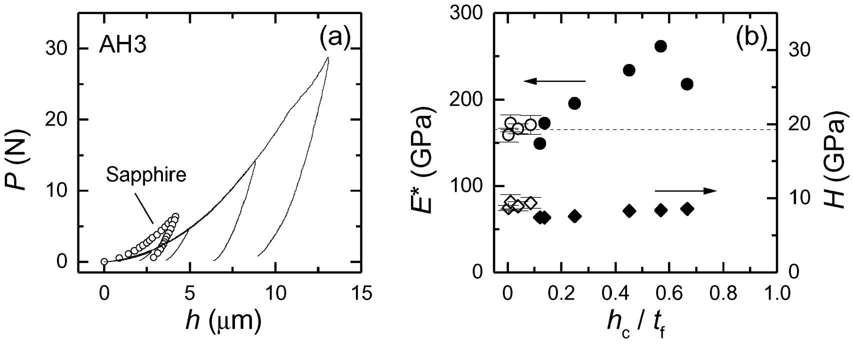

Figure 8 Depth-sensing indentation of AH3. (a) Macroindentation *P-h* traces. Also shown is a *P-h* trace of (0001) sapphire for comparison (open squares). (b) Plane-strain modulus E^* and hardness H with increasing relative contact depth h_c/t_f. Open circles are moduli obtained by nanoindentation and solid circles by macroindentation. Open diamonds are hardness obtained by nanoindentation and solid diamonds by macroindentation. The dashed line shows the value of plane-strain modulus taken as representative for the film.

TABLE I Alumina film mechanical properties

					Thermal stress	
Specimen ID	Modulus, E (GP$_a$)	Hardness, H (GP$_a$)	Toughness, T (MPa m$^{1/2}$)	Interfacial fracture resistance, R (J m^{-2})	Peak temp, T_P (°C)	CTE, α (ppm K^{-1})
AH1	–	8.0[c]	1.8 ± 0.1[c]	–	100	7.6 ± 0.9
					200	7.5 ± 0.3
					300	7.4 ± 0.5
					400	7.4 ± 0.2
					500	7.3 ± 0.2
AH2	–	–		–	300	7.5 ± 0.1
AH3	158[a]	7.3[d]	2.1 ± 0.3	0.9 ± 0.1	–	–
AH4	93[b]	–	–	–	300	7.4 ± 0.2
AH5	–	–	–	–	300	7.0 ± 0.4
AH6	–	–	–	–	–	–
Si1	93[b]	–	–	–	300	5.8 ± 0.1
						7.1 ± 0.3[b]
AL1	174[a]	7.9[d]	1.7 ± 0.5	1.1 ± 0.1	–	–
AL2	–	–	–	–	300	6.9 ± 0.3
AL3	–	–	–	–	300	6.9 ± 0.2
AL4	–	–	–	–	300	6.7 ± 0.7

[a] From DSI.
[b] From double-substrate.
[c] Vickers indentation, post-anneal.
[d] Vickers indentation, as-deposited.

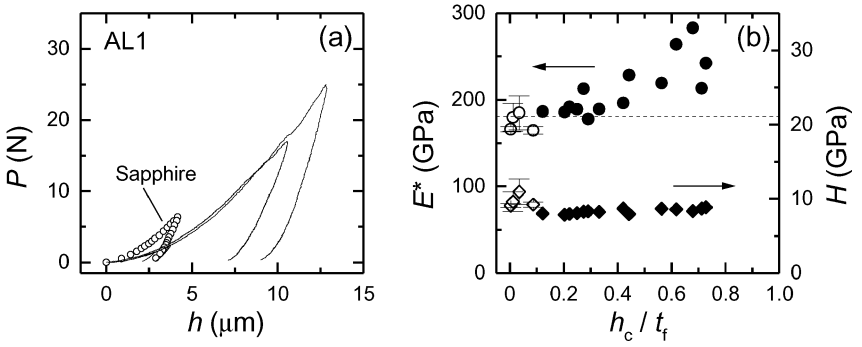

Figure 9 Depth-sensing indentation of AL1. (a) Macroindentation *P-h* traces. Also shown is a *P-h* trace of (0001) sapphire for comparison (open squares). (b) Plane-strain modulus E^* and hardness H with increasing relative contact depth h_c/t_f. Open circles are moduli obtained by nanoindentation and solid circles by macroindentation. Open diamonds are hardness obtained by nanoindentation and solid diamonds by macroindentation. The dashed line shows the value of plane-strain modulus taken as representative for the film.

consistently lower than the CTE of the films deposited at a substrate bias of −130 V (neglecting Si1).

The CTE and modulus obtained from the double-substrate method in Part I are different from the values obtained using DSI results (Table I). The discrepancy may be explained by the thermal stress observations of Part I. Because Si1 exhibited less stress development (magnitude) during annealing, it is closer to its equilibrium structure at 300°C. Consequently the linear stress-temperature response during cooling is the response of an AlO$_x$ film nearly at equilibrium, in contrast to films on Al$_2$O$_3$-TiC substrates that were further from equilibrium during the anneal and subsequent cool-down. Thus the fundamental assumption of the double-substrate method was invalid and, in principal, it cannot provide any useful information. (In this case, however, it served to highlight the structural dependence of the films on the magnitude of stress during annealing.) Further, the CTE obtained from the linear stress-temperature response of Si1 following the anneal and DSI results from AH3 is significantly less than that obtained for any films on Al$_2$O$_3$-TiC substrates. The CTE of an AlO$_x$ film (nearly) in its equilibrium state is reduced from that of a film in its as-deposited state. This is supported by the decrease in CTE observed with increased thermal cycling in AH1 (Table I). As the film was thermal cycled (already shown to be effectively the same as annealing in Part I) its structure approached its equilibrium state, resulting in a decrease in CTE, as previously observed in PECVD silicon oxide films [35].

The ratio of the final depth to the maximum depth ε, extracted from the *P-h* traces, was found to be constant with the depth of indentation as shown in Fig. 10a for AH3 and Fig. 10b for AL1. For AH3, $\varepsilon = 0.63 \pm 0.05$ and for AL1 $\varepsilon = 0.65 \pm 0.02$. As shown in Equation 9, ε relates the displaced indentation volume at peak load to the residual displaced volume after complete unload and elastic recovery. The residual displaced volume is a function of the film hardness and as the hardness of AH3 and AL1 are within 10% of each other, it is not surprising that ε is not significantly different. The invariance

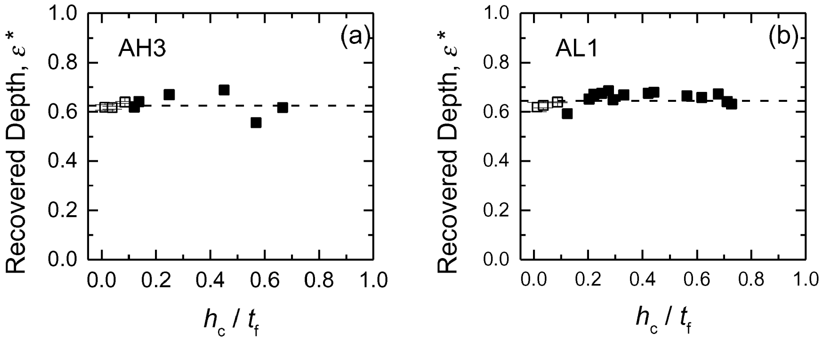

Figure 10 Recovered depth, ε, with increasing relative contact depth for (a) AH3 and (b) AL1, measured by nanoindentation (open symbols) and macroindentation (closed symbols).

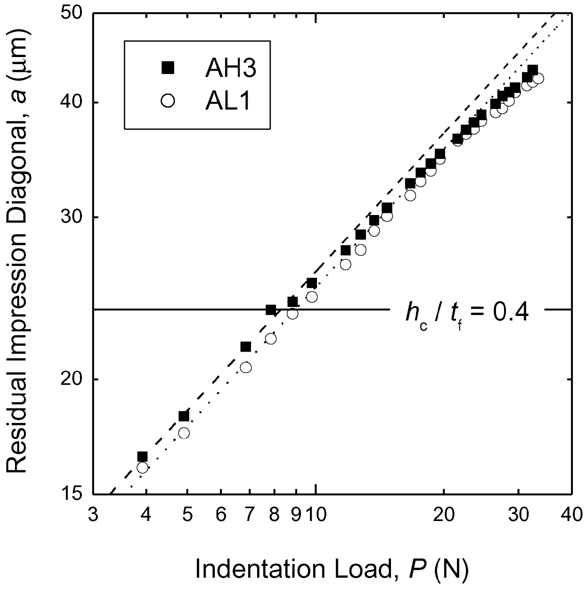

Figure 11 Residual impression diagonal with increasing indentation load on AH3 (solid squares) and AL1 (open circles). The dashed and dotted lines are for $H = 7.3$ GPa and 7.9 GPa for AH3 and AL1, respectively.

of ε with contact depth is also expected because H was virtually constant with contact depth.

4.2. Vickers indentation

4.2.1. Hardness and film cracking

Vickers indentation was performed on AH1 following the heat treatment to a peak temperature of 500°C, as described in Part I, on the half of the film still intact. Indentations in the load range $0.1 < P < 10$ N were performed to determine the plastic and fracture properties of the film. The residual impression diagonal length $2a$ and equilibrium radial crack length c_0 were measured directly by post-indentation optical microscopy. For 10 N indentations the residual impression diagonal $a = 25$ μm, which corresponds to $h_c/t_f \approx 0.14$ for an ideal Vickers tip. For loads under 10 N, it is then expected that both the plastic zone and film cracks should be fully developed hemi-spheres and radials, as in a homogeneous material. The measured hardness, $H = 8.0$ GPa, is greater than that measured on as-deposited AH3 (Section 4.1 and below), indicating that the heat treatment changed not only the stress state and CTE but also the plastic contact response of the film. Assuming E_f did not change during the heat treatment and using $\sigma_f = -225$ MPa (Part I) in Equation 6 results in $T = 1.8 \pm 0.1$ MPa m$^{1/2}$. This toughness is below the range for polycrystalline alumina, $T = 2 - 10$ MPa m$^{1/2}$ [11].

Fig. 11 is a logarithmic plot of the residual impression diagonal a with increasing indentation load P for AH3 and AL1. The difference between the two films is slight, confirming the small difference in H measured by DSI. The effect of the substrate is seen as a deviation from the $a \sim P^{1/2}$ relationship arising from the assumption of constant hardness. Because the substrate is significantly harder than the film, a is smaller than expected as the indenter approaches the substrate. The deviation occurs approximately at $a = 24$ μm, which corresponds to $h_c/t_f = 0.4$, shown as a solid horizontal line on Fig. 11. The film hardness was obtained from a linear fit of slope 1/2 to the data for $a < 24$ μm to obtain $H = 7.3$ and 7.9 GPa for AH3 and AL1, respectively, in agreement with (macroscopic scale) DSI results and are included in Table I. The fits are included in Fig. 11.

Fig. 12 is a logarithmic plot of the equilibrium crack length c_0 with increasing impression diagonal a for AH3 and AH6. Focusing on AH3, the crack lengths approximately follow the $c_0 \sim a^{4/3}$ trend of fully-developed radial cracks in homogeneous materials for $a < 25$ μm ($h_c/t_f < 0.4$). As a increases c_0 passes through a transition period until at $a > 34$ μm ($h_c/t_f > 0.6$) the data follow the $c_0 \sim a^4$ trend predicted in this analysis for channel cracks. Note that the approximate $c_0 \sim a^{4/3}$ trend continues until approximately the same relative contact depth ($h_c/t_f < 0.4$) as the constant film H behaviour of Fig. 11. (The crack lengths do not follow the $c_0 \sim a^{4/3}$ trend exactly due to the effects of film stress—Equation 7.) The dashed line of approximate slope 4/3 in Fig. 12 is a best-fit of Equation 7 to AH3 data points for $a < 25$ μm. Assuming $\sigma_f = -41$ MPa (Part I), $\varepsilon = 0.63$ and $\psi = 1.3$ (using the measured E_f to calculate the Dundur's parameters [18]) results in $T = 2.1 \pm 0.3$ MPa m$^{1/2}$. A best-fit of Equation 16 to the data points for $a > 34$ μm is also included in Fig. 12 as a dashed line. From Equation 16 assuming $\sigma_f = -41$ MPa and $\psi = 1.3$ the parameter λ was evaluated to be 0.016 ± 0.003. A second dashed line of slope four in Fig. 12 resulted from a best-fit of Equation 16 to the data of AH6 for $a > 20$ μm. From

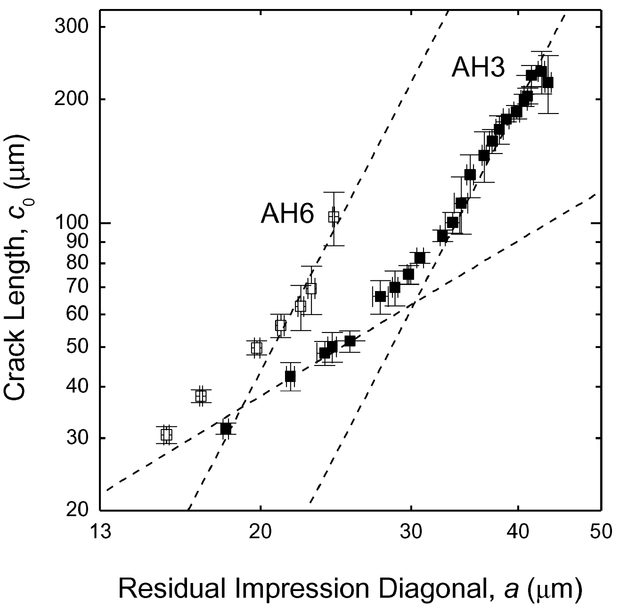

Figure 12 Crack length (radial or channel) with increasing residual impression size for AH3 and AH6 (solid and open squares, respectively). Best-fit lines from Equations 7 and 16 are included for AH3 as dashed lines for $a < 25$ μm and $a > 34$ μm, respectively. A best-fit line from Equation 16 is included for AH6 for $a > 20$ μm.

Equation 16 assuming $\sigma_f = -41$ MPa and $\psi = 1.3$ the parameter λ was evaluated to be 0.014 ± 0.002. The constant λ obtained from channel cracking in AH3 and AH6 is nearly the same, implying that the channel cracking model developed here scales with film thickness correctly.

Fig. 13 shows equilibrium crack length measurements taken on AL1. As with AH3 and AH6, c_0 goes through a transition from radial to channel cracking with increasing indentation load. From a best-fit of Equation 7 to the data points for $a < 24$ μm (dashed line), using $\sigma_f = -37$ MPa (Part I), $T = 1.7 \pm 0.5$ MPa m$^{1/2}$ (Table I). The dashed line of slope four in Fig. 13 results from a best-fit of Equation 16 to the data for $a > 34$ μm. Assuming $\sigma_f = -37$ MPa, $\psi = 1.3$, and $T = 1.7$ MPa m$^{1/2}$ results in $\lambda = 0.013 \pm 0.006$, close to the value determined for the high bias film. The invariance of λ with thickness and material type suggested by Equation 13 further supports the validity of the channel crack model.

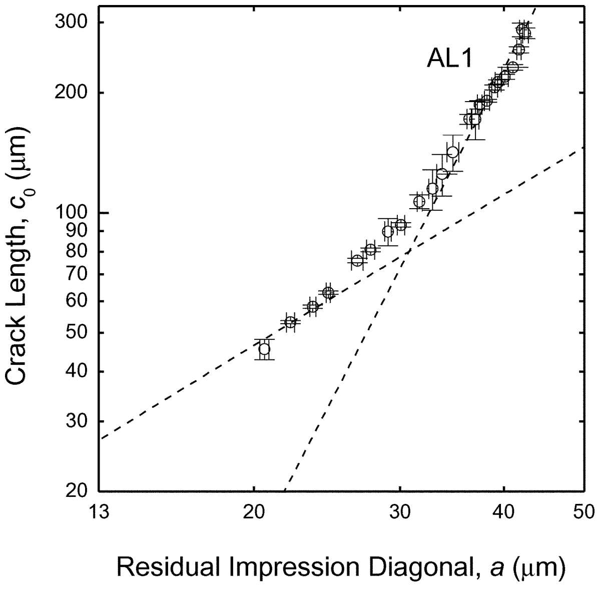

Figure 13 Crack length with increasing residual impression size for AL1. Included are best-fit lines from Equations 7 and 16 as dashed lines for $a < 25$ μm and $a > 34$ μm, respectively.

The maximum indentation loads used in this study were limited by film spalling and chipping. An example of this is shown in Fig. 1e. The interference fringes in the debonded region make it easy to see where the film has completely spalled off the substrate (the right half of the region) and the Al_2O_3-TiC underneath the debonded region is visible. Close inspection of this indentation (and many others) revealed that the Al_2O_3-TiC substrate was not cracked, providing experimental evidence for the assumption made in Section 2.2; that the radial cracks do not enter the substrate but instead are confined to the film and turn into channel cracks at large loads.

4.2.2. Interfacial cracking

The interference fringes surrounding the residual indentation impressions of Fig. 1 are indicative of interfacial cracking beneath the indentation. The presence of an air gap between the film and substrate in the circular debond region surrounding the indentation impression is unmistakable, but it is not clear from Fig. 1 whether the debonded region is buckled or merely delaminated. Buckling provides an additional driving force for interfacial cracking, enhancing the compressive film stress. Some large indentations in which interfacial cracking occurred on AH3 and AL1 were coated with about 50 nm of Au by evaporation and the debonded regions examined by profilometry and interferometry. Both techniques indicated the debonded regions had an aspect ratio of 1:100, i.e., a debonded region 100 μm in diameter was displaced vertically about 1 μm from the interface in the centre near the indentation impression. This aspect ratio is too small for a buckled clamped circular plate. For a 17 μm film, if the indentation stress plus the compressive film stress is 20% greater than the critical buckling stress then the vertical displacement from the interface at the centre of the buckle would be 11 μm [36]. The greatest centre displacement of a debond region in either AH3 or AL1 was measured to be 5 μm at a load of 32 N, the largest load used in this analysis. For this indentation load, the critical buckling stress is 607 MPa while the effective edge stress is calculated to be 240 MPa, less than half the stress required for buckling (Equations 24 and 25). The measured aspect ratios of the debonded regions and the calculated effected edge stresses suggest that no buckling occurred at any indentation loads used here.

Fig. 14 shows the measured interfacial crack parameter vs. residual impression diagonal measured on AH3, AH6, and AL1 in the form suggested by Equation 20. (The interfacial crack radii were deduced by measuring the debonded area and assigning an effective radius, although direct measurements of the debond diameter were about the same.) Focusing on AH3 and

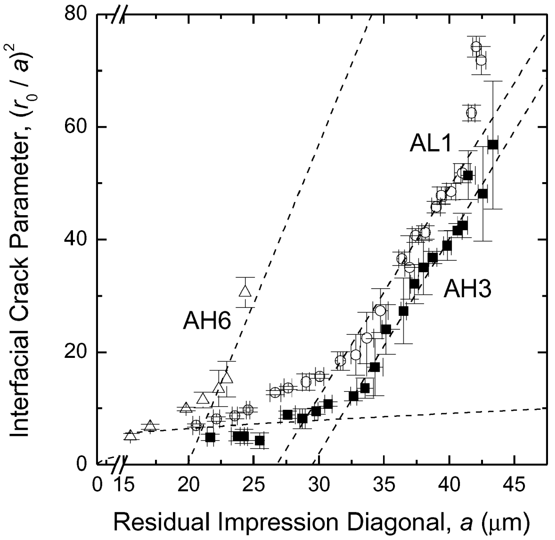

Figure 14 Interfacial crack parameter variation with increasing residual impression diagonal for AH3, AH6, and AL1. The data for AH3 and AL1 clearly separates into two regions: For $a < 32$ μm the interfacial crack parameter has a weak dependence on indentation load and for $a > 34$ μm the dependence is stronger and linear. Best-fit lines are included for AH3 and AL3, as is the predicted response of AH6. The trend at small a is described by a line representing $r_0 \sim a^{5/4}$, as predicted for lateral cracks.

AL1, the data for both films are split into two regions: for $a < 32$ μm the interfacial crack parameter $(r_0/a)^2$ varies slowly with increasing a. For $a > 34$ μm $(h_c/t_f > 0.6)$ the interfacial crack parameter is linear in a. As before, the transition point in Fig. 14 is thought to be caused by a change in the geometry of the plastic zone from spherical to cylindrical. Once the plastic zone becomes cylindrical in shape, the data are well described by Equation 20. This transition point is the same as the transition point identified for channel cracks. (This is consistent with the assertion that radial cracks are about the same depth as the bottom of the plastic zone, so they change geometry due to the substrate influence at approximately the same value of a.) A dashed line corresponding to $r_0 \sim a^{5/4}$ or $(r_0/a)^2 \sim a^{1/2}$ (Equation 17) is included in Fig. 16 for lateral cracking and appears to capture the general trends of all three films at low loads.

Also included in Fig. 14 are best-fit lines to the data for $a > 34$ μm for AH3 and AL1. According to Equation 20, the slope of the lines provides information regarding R and the intercept provides information about the b/a scaling of Equation 16: the constant d_3 was calculated to be 2.1 ± 0.1 for AH3 and 1.9 ± 0.1 for AL1. In Section 2.2 it was asserted that d_3 must contain information about the hardness and stiffness mis-match between the film and substrate. The hardness and moduli of the two films differ by only 10%, so the b/a scaling relationship (and d_3) should be about the same for both films. The fracture resistance can be calculated to within a constant term from the slopes of the best-fit lines: for AH3, $R/\Lambda^2 = 680 \pm 70$ J m^{-2} and for AL1, $R/\Lambda^2 = 790 \pm 80$ J m^{-2}, indicating that the AL1 actually adheres at least as well, if not better, to Al_2O_3-TiC than AH3. The fact that the debond radius for AL1 at a given a is greater than the debond radius in AH3 is due to its greater modulus, which causes the plastic zone for a given a to exert significantly more pressure on the film than in AH3 (see Equation 10). The interfacial fracture resistance can be related further to the parameter d_1, expected to be of the order one, using Equation 21: for AH3, $R/d_1^2 = 0.9 \pm 0.1$ J m^{-2} and for AL1, $R/d_1^2 = 1.1 \pm 0.1$ J m^{-2} (included in Table I assuming $d_1 = 1$). These estimates of the interfacial fracture resistance can be compared to the cohesive fracture resistance of polycrystalline alumina, $R = 10$–250 J m^{-2} [11]. If the Al_2O_3 of the substrate comprises 64% of the surface area and AlO_x adheres perfectly to the Al_2O_3 phase but not at all to the TiC phase, then the fracture resistance of the interface would be expected to be 6.4 J m^{-2} (on the low end of the range). The measured values of R/d_1^2 are therefore of the expected order of magnitude. Also included in Fig. 14 are data for AH6 and the predicted variation in the interfacial crack parameter using $R/\Lambda^2 = 680$ J m^{-2}. The measured interfacial crack lengths are predicted well at the three loads where the model applies ($a > 20$ μm). The model of Marshall and Evans [22] could not be applied to the measured delamination radii in this study, as Equation 22 did not well describe the r_0 vs. a data over the indentation load range examined here.

5. Summary

The thermo-mechanical, elastic, plastic, fracture, and interfacial properties of non-reactive sputtered AlO_x films of varying thickness on Al_2O_3-TiC substrates deposited at two different substrate biases were examined by a variety of mechanical characterization techniques. The films were deposited in compression and film stress measurements on thermal cycling identified an irreversible increase in compressive stress during cycling and annealing at elevated temperatures. The thermo-mechanical response was independent of film thickness (between 5 and 50 μm) and substrate bias used during deposition. The permanent change in stress was accompanied by a slight increase in hardness and decrease in film CTE. Depth-sensing indentation was used to determine film modulus and hardness, both of which were significantly reduced from those for polycrystalline alumina. The modulus and hardness of the film deposited at a substrate bias of −50 V was found to be slightly greater than that of the film deposited at a substrate bias of −130 V. For films deposited at both substrate biases, the ratio of recovered volume during unloading to the displaced volume at peak load was found to be independent of indentation depth.

Vickers indentation induced film and interfacial fracture above a threshold load. Thick films were indented to identify the film toughness based on known analysis methods for radial cracking. Indentation on thinner films resulted in channel cracking. A new model treating the channel cracks as line-loaded one-dimensional cracks correctly predicted the $c_0 \sim a^4$ relationship and accurately captured the effect of decreasing film thickness. Interfacial fracture was modelled in a similar manner using a previously published solution for the mechanical energy release rate of an axi-symmetric edge-loaded crack. The model correctly predicated the linear relationship between $(r_0/a)^2$ and a and was able to determine the mechanical energy release rate of interfacial fracture to within a constant. This model also correctly predicted the effect of decreasing film thickness. The fracture properties of the films, in terms of toughness T and interfacial crack resistance R, deposited at substrate biases of -50 and -130 V were found to be (statistically) the same.

References

1. J. THURN and R. F. COOK, *J. Mater. Sci.* (this volume).
2. J. THURN and R. F. COOK, *J. Mater. Res.* **17** (2002) 2679.
3. R. F. COOK and G. M. PHARR, *J. Amer. Ceram. Soc.* **73** (1990) 787.
4. W. C. OLIVER and G. M. PHARR, *J. Mater. Res.* **7** (1992) 1564.
5. Y. SUN, T. BELL and S. ZHENG, *Thin Solid Films* **258** (1995) 198.
6. J. L. HAY, M. E. O'HERN and W. C. OLIVER, "Mat. Res. Soc. Symp. Proc" (MRS, Pittsburgh PA, 1998) Vol. 522, p. 27.
7. W. ZHANG and G. SUBHASH, *Int. J. Solids Struc.* **38** (2001) 5893.
8. B. R. LAWN, A. G. EVANS and D. B. MARSHALL, *J. Amer. Ceram. Soc.* **63** (1980) 574.
9. M. T. LAUGIER, *ibid.* **68** (1985) C-51.
10. R. F. COOK, Ph.D. Thesis, School of Physics, University of New South Wales, Australia, 1985.
11. B. LAWN, "Fracture of Brittle Solids," 2nd ed. (Cambridge University Press, Cambridge, 1993) p. 31, 55.
12. A. GOLDSTEIN and A. SINGURINDI, *J. Amer. Ceram. Soc.* **83** (2000) 1530.
13. I. Y. KONYASHIN, *J. Vac. Sci. Technol.* A **14** (1996) 447.
14. R. F. COOK, *J. Amer. Ceram. Soc.* **77** (1994) 1263.
15. H. TADA, P. C. PARIS and G. R. IRWIN, "The Stress Analysis of Cracks Handbook" (Del Research Corp., St. Louis, MO, 1973) p. 2.22.
16. R. HILL, "The Mathematical Theory of Plasticity" (Oxford University Press, London, 1950) p. 106.
17. M. D. THOULESS, *J. Vac. Sci. Technol.* A **9** (1991) 2510.
18. J. W. HUTCHINSON and Z. SUO, *Adv. Appl. Mech.* **29** (1992) 63.
19. D. B. MARSHALL, B. R. LAWN and A. G. EVANS, *J. Amer. Ceram. Soc.* **65** (1982) 561.
20. M. D. THOULESS, *Acta Metall.* **36** (1988) 3131.
21. A. A. GRIFFITH, *Phil. Trans. Roy. Soc. London Ser.* A **221** (1921) 163.
22. D. B. MARSHALL and A. G. EVANS, *J. Appl. Phys.* **56** (1984) 2632.
23. A. G. EVANS and J. W. HUTCHINSON, *Int. J. Solids Struct.* **20** (1984) 455.
24. C. ROSSINGTON, A. G. EVANS, D. B. MARSHALL and B. T. KHURI-YAKUB, *J. Appl. Phys.* **56** (1984) 2639.
25. M. D. KRIESE, W. W. GERBERICH and N. R. MOODY, *J. Mater. Res.* **14** (1999) 3019.
26. J. THURN and R. F. COOK, *J. Mater. Res.* **17** (2002) 1143.
27. J. MENCÍK, D. MUNZ, E. QUANDT, E. R. WEPPELMANN and M. V. SWAIN, *ibid.* **12** (1997) 2475.
28. T. Y. TSUI and G. M. PHARR, *ibid.* **14** (1999) 292.
29. T. Y. TSUI, J. VLASSAK and W. D. NIX, *ibid.* **14** (1999) 2196.
30. Y. XU, Y. TSAI, D. W. ZHENG, K. N. TU, C. W. ONG, C. L. CHOY, B. ZHAO, Q.-Z. LIU and M. BRONGO, *J. Appl. Phys.* **88** (2000) 5744.
31. Y. TOIVOLA, J. THURN and R. F. COOK, *J. Electrochem. Soc.* **149** (2002) F9.
32. J. B. PETHICA, R. HUTCHINGS and W. C. OLIVER, *Phil. Mag.* A **48** (1983) 593.
33. M. F. DOERNER and W. D. NIX, *J. Mater. Res.* **1** (1986) 601.
34. T. C. CHOU, T. G. NIEH, S. D. MCADAMS and G. M. PHARR, *Scr. Metall. et Mater.* **25** (1991) 2203.
35. J. THURN and R. F. COOK, *J. Appl. Phys.* **91** (2002) 1988.
36. J. W. HUTCHINSON, M. D. THOULESS and E. G. LINIGER, *Acta Metall. Mater.* **40** (1992) 295.

Received 4 November 2003
and accepted 6 April 2004